Synthesis and Spectroscopy of Lanthanide Ion-doped Y_2O_3

Peter A. Tanner* and Ka Leung Wong

Department of Biology and Chemistry, City University of Hong Kong, Tat Chee Avenue, Kowloon, Hong Kong SAR, People's Republic of China

Received: June 5, 2003; In Final Form: October 22, 2003

The preparation of $Y_2O_3:Ln^{3+}$ (Ln = Eu, Er; nominal 1−0.1 mol % doping) by the preformed sol method is reported. The comparison of the emission spectra with more concentrated samples prepared by flame spray pyrolysis and conventional spray pyrolysis shows that emission from $^5D_1$ is quenched in the latter samples, and C_{3i} site emission is relatively weaker, when compared to C_2 site emission. Experimental data are provided to dispute the recent reassignments of the energy levels of Eu^{3+} situated at C_{3i} sites in Y_2O_3. The comparison of the emission spectrum of micrometer-scale $Y_2O_3:Er^{3+}$ with that previously reported for nanoscale material shows a significant enhancement of hot bands in the latter. The enhanced population of $^2H_{11/2}$ leads to rather different behavior in the energy transfer phenomena of the nanoscale material.

Introduction

There is a considerable amount of interest in the emission of $Y_2O_3:Eu^{3+}$, since it is a widely used red phosphor and display material,[1−8] and more recently, particular attention has been paid to the luminescence properties of nanocrystalline $Y_2O_3:Eu^{3+}$.[9−17] In this paper the luminescence of this powder prepared by some different preparative techniques is compared, and some outstanding and controversial issues in the spectroscopy of $Y_2O_3:Ln^{3+}$ are resolved.

Micrometer-size Y_2O_3 crystallizes as the *C*-type (space group $Ia3 - T_h^7$, $Z = 16$), and there are 24 C_2 sites and eight $S_6 \equiv C_{3i}$ sites for Y^{3+} in the unit cell.[18] Both types of site comprise Y^{3+} ions in octahedral coordination to oxygen, at the center of a cube. In the former, the missing two oxygens are on a face diagonal, whereas for the latter they lie on a body diagonal. The emission spectra of Eu^{3+}-doped Y_2O_3 have been utilized to provide energy level data for crystal field analysis, with the site symmetry being taken as C_2[19] but not far from C_{2v}.[18] The luminescence spectra and energy levels of the C_{3i} system have recently been reinvestigated and reassigned from theoretical arguments,[3,8,20] and we present experimental evidence to show that the original assignments are correct.

A preliminary report has been made of the chemical and structural characterization of powders prepared from Y_2O_3 preformed sol (PS),[21] together with the low-resolution luminescence of $Y_2O_3:Er^{3+}$ powders. This PS route, from nanometer-scale dispersed particles of Y_2O_3, is rapid and inexpensive, but the particles produced are irregular in size and morphology. Conventional spray pyrolysis (CSP)[22] is an alternative preparative technique, which produces small, spherical particles. A metal salt is used as precursor (with or without flux) and dry air is employed as a carrier gas. The solution is atomized by an ultrasonic spray generator and introduced into a hot reaction column. The resulting particles are then collected on a suitable substrate. The particle size is determined by the concentration of the precursor solution and the droplet size from the ultrasonic nebulizer. The disadvantage of the process is that hollow particles are produced that have poor mechanical and thermal stability. The general flame spray pyrolysis (FSP) system consists of an ultrasonic nebulizer, a flame nozzle, a quartz reactor, a bag filter, and a pump. The evaporation, decomposition, crystallization, and melting of droplets, with oxygen or air in the high-temperature flame at 1200−2000 °C, is followed by rapid quenching to produce dense and spherical particles without agglomeration. The concentration of the precursor solution directly influences the particle size. One aim of this study was to compare the high-resolution luminescence properties of $Y_2O_3:Eu^{3+}$ powders synthesized by these three different methods. Preferential site occupation and dopant ion concentration have previously been investigated for $Y_2O_3:Eu^{3+}$.[23]

Y_2O_3 doped with Er^{3+} has also been prepared by the PS method, and the high-resolution luminescence has been recorded for a check of the purity of this material. This led us to compare the spectra with the results of previous studies and to comment upon the luminescence and energy transfer behavior of bulk and nanocrystalline $Y_2O_3:Er^{3+}$ because some aspects are unresolved in previous studies.[24,25]

It has been argued from magnetic susceptibility measurements that only the C_2 sites in Y_2O_3 are occupied at low concentrations of Ln^{3+}.[26] X-ray diffraction data from cubic $Y_2O_3:Gd^{3+}$ show that at concentrations ≤20% Gd^{3+}, the guest occupies exclusively the C_2 sites, but at higher concentrations the occupation of C_{3i} sites increases continuously.[27] By contrast, from X-ray powder diffraction and magnetic susceptibility studies of $Y_2O_3:Eu^{3+}$ (between 5 and 90 mol % Eu^{3+}), Antic et al.[28] found no significant partitioning of Eu^{3+} ions between the C_{3i} and C_2 sites. Mössbauer investigations of nanocrystalline $Y_2O_3:Eu^{3+}$ (10 mol % Eu^{3+}) indicated ∼50% occupancy each of C_2 and C_{3i} sites, so that the higher symmetry site is preferentially occupied.[29] However, from measurements of the reflection spectra of $Y_2O_3:Eu^{3+}$ at different concentrations (≥1%) of Eu^{3+}, it is clear that the guest Ln^{3+} ions enter the sites in $Y_2O_3:Ln^{3+}$ in a random manner,[19] at least for high-temperature preparations.[30]

Experimental Section

$Y_2O_3:Eu^{3+}$ was prepared by three different methods. First, the PS method[21] utilized colloidal Y_2O_3 (14% by mass Y_2O_3; nominal 2.5 nm particle size; obtained from PQ Corporation) dispersed in acetate solution at pH 7. The sol was mixed with

10.1021/jp035583o CCC: $27.50
Published on Web 11/25/2003

TABLE 1: Description of Eu^{3+}-Doped Y_2O_3 Products

preparation method	nominal (EDX) Eu^{3+} concn, at. %	sample label
preformed sol	0.1	PS0.1
preformed sol	1.0 (0.5)	PS1
conventional spray pyrolysis	6.0	CSP
flame spray pyrolysis		
0.1 M	6.0 (1.5)	FSP0.1
0.3 M	6.0	FSP0.3
0.5 M	6.0	FSP0.5
1.0 M	6.0 (2.0)	FSP1
2.0 M	6.0	FSP2

the appropriate amount of $Eu(NO_3)_3$ solution (prepared from Eu_2O_3, Strem, 99.999%) together with about 1% by mass of 1.0 M HNO_3 (Reidel-de-Haën). An opaque gel formed after about 1 h, which was subsequently heated at 80 °C for 4 h in a vacuum oven and then at 1200 °C for 12 h. The Eu^{3+} dopant ion concentrations were 1 and 0.1 mol %. Y_2O_3:Er^{3+} was similarly prepared.

Samples were also prepared by CSP as in ref 31, and by FSP, using precursor solutions containing $Y(NO_3)_3$ and $Eu(NO_3)_3$ of several different concentrations between 0.1 and 2.0 M, as labeled in Table 1, and then annealed at 1200 °C for 5 h. The Eu^{3+} doping concentration was 6 at. %.[32] In the present study, the CSP and FSP samples were aged for several months, whereas the PS samples were freshly prepared. We therefore did not directly compare the relative emission intensities for these two different groups since surface defects are more likely to occur for the former samples.

Emission spectra were recorded at temperatures down to 10 K at a resolution of 1−2 cm^{-1} by use of argon ion laser excitation and the equipment previously described.[33] Scanning electron micrographs were recorded on an ESEM XL 30 Phillips electron microscope.

SEM Characterization of Products. Figure 1 shows the SEM micrographs of selected samples. The mean particle sizes were estimated by measuring ∼100 particles. The preformed sol sample PS1 consists of sheets of irregularly shaped particles with sizes ranging from several hundred nanometers to several micrometers, with mean size 340 ± 310 nm. The CSP sample, Figure 1b, comprises separate, hollow spheres, many of which are fractured, with diameters varying by a factor of about 7, and mean value 1.37 ± 0.65 μm. Figure 1 panels c and d show the products FSP0.1 and FSP 1, which consist of spherical particles of mean diameters 540 ± 270 nm and 810 ± 300 nm, respectively. The EDX results for the atomic percent of Eu in the selected particles (Table 1, column 2, in parentheses) are between 2 and 4 times lower than the nominal concentrations.

Luminescence of Y_2O_3:Eu^{3+}. The energy levels of Eu^{3+} in Y_2O_3 deduced by Leavitt et al.[19] are shown for reference in Figure 2. Although the intraconfigurational f−f transitions of Eu^{3+} are electric dipole- (ED-) forbidden in the free ion, they are allowed by the forced ED mechanism[34] at a C_2 site. The free ion selection rules for magnetic dipole (MD) transitions are $\Delta S = 0$, $\Delta L = 0$, and $|\Delta J| \leq 1$; $J = 0 \leftrightarrow J = 0$ and $L = 0 \leftrightarrow L = 0$ are forbidden, so that the $^5D_0 \leftrightarrow {}^7F_1$ transition is prominent. With the exception of the latter MD transition, the spectra of Eu^{3+} ions at C_{3i} sites are expected to be ED vibronic in character, since the site centrosymmetry does not permit forced ED transitions. Although f−f transitions are potentially MD-allowed at the C_{3i} site, which are forbidden in octahedral symmetry, this intensity contribution is expected to be weak.

Comparison of Emission Spectra for Different Preparations of Y_2O_3:Eu^{3+}. Figure 3 shows the 10 K $^5D_0$ emission spectrum of the sample FSP1 under 457.9 and 488 nm excitation. In each case, the excitation is off-resonance and into weak vibronic structure. The emission from $^5D_0$ is stronger under the former wavelength because the excitation energy is ca. 321

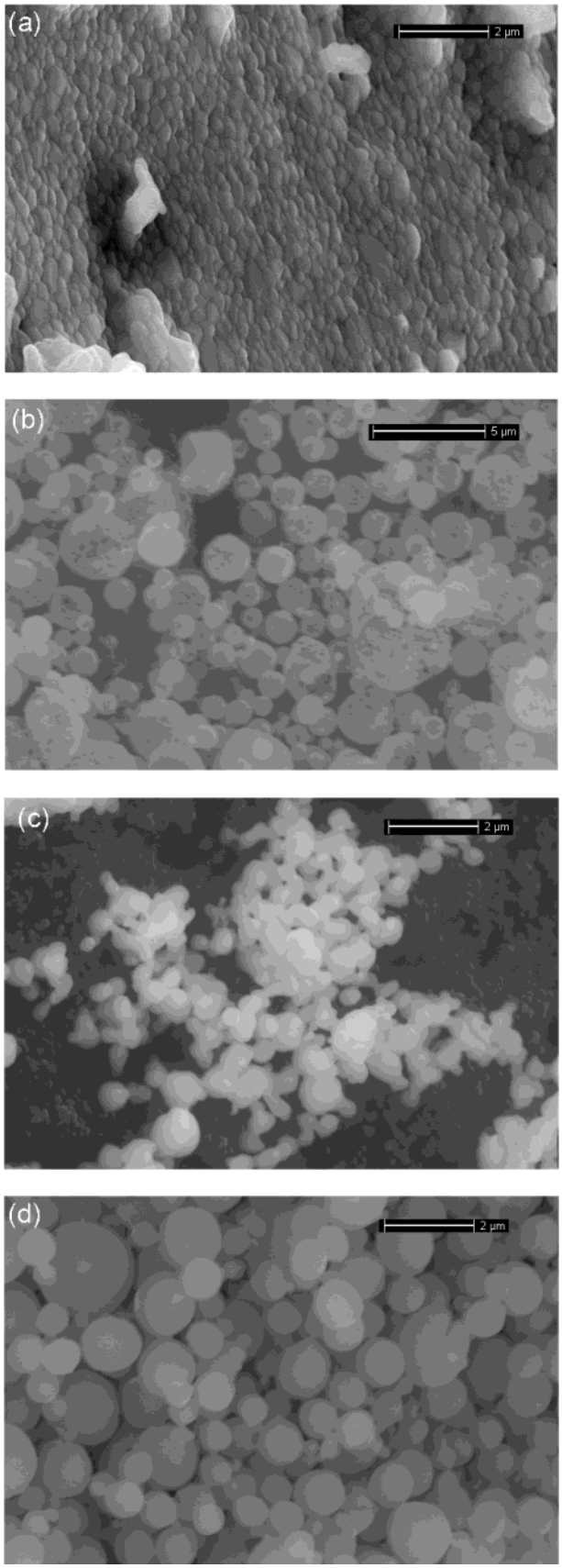

Figure 1. SEM micrographs of selected Y_2O_3:Eu^{3+} samples: (a) PS1, (b) CSP, (c) FSP0.1, and (d) FSP1. The markers in panels a, c, and d are 2 μm; in panel b, 5 μm.

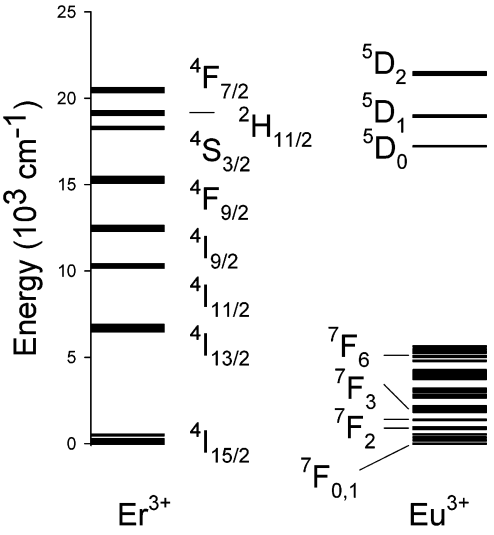

Figure 2. Energy levels below 22 000 cm^{-1} of Er^{3+} and Eu^{3+} in Y_2O_3 from literature data (refer to the text)

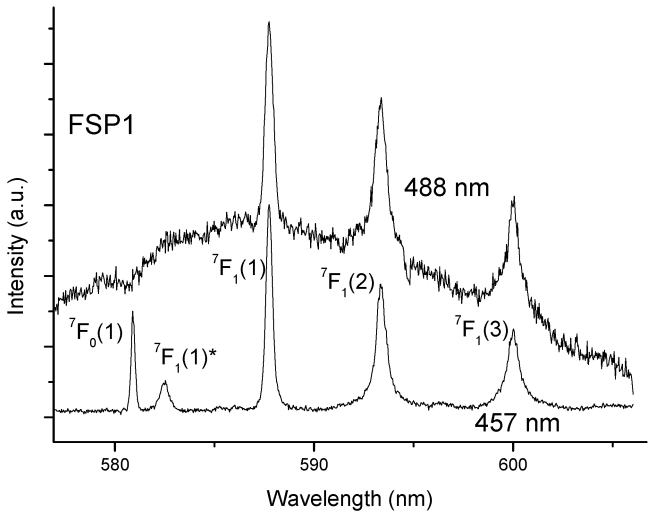

Figure 3. Emission spectra (at 10 K) of FSP1 between 575 and 605 nm under 457.9 and 488 nm excitation. The initial state is $^5D_0$ and the terminal ^7F levels are labeled in increasing order of energy in the parentheses, without and with an asterisk for the C_2 and C_{3i} sites, respectively.

cm^{-1} (one phonon) above an electronic energy level, whereas it is ca. 1490 cm^{-1} (three phonons) above for 488 nm excitation. The background scattering is greater under 488 nm excitation, and self-absorption occurs for features coincident in emission and absorption. The bands are labeled with numerals according to increasing energy of the terminal states (with total degeneracy $2J + 1$, i.e., 1 for $^7F_0$, 3 for $^7F_1$) for the C_2 site. Features corresponding to the C_{3i} site are starred. Consistent with previous studies, where lifetime measurements have been performed,[23,35] the band at 582.6 nm is assigned to one of the two C_{3i} components of $^7F_1$.

Figure 4 shows the same spectral region at room temperature, under 488 nm excitation, and compares the relative emission intensities for all of the FSP and CSP samples. The emission intensity is lowest for CSP and highest for the FSP1 sample. The same results are found for other spectral regions and for 457.9 nm excitation. The FSP particles prepared from higher precursor concentrations have larger particle size, and it is evident that there is an optimum size (near 1 μm in this case) for the highest luminescence intensity. The room-temperature spectra of the PS samples in this spectral region are rather

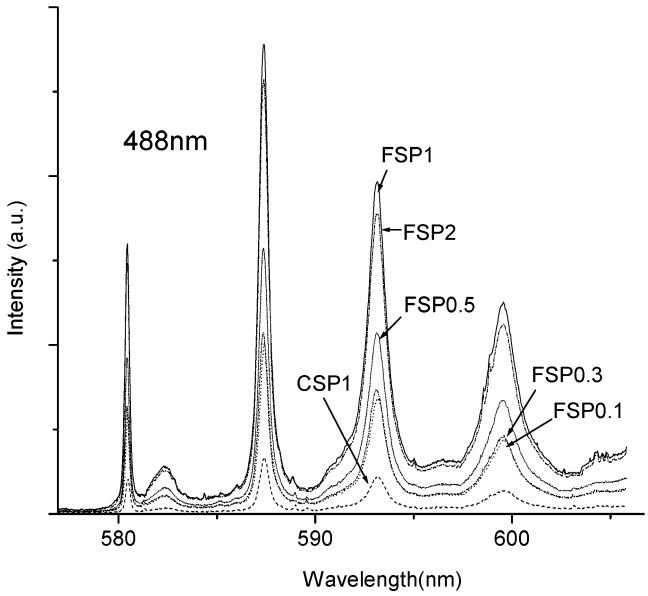

Figure 4. Room-temperature 488 nm excited emission spectra of FSP and CSP samples.

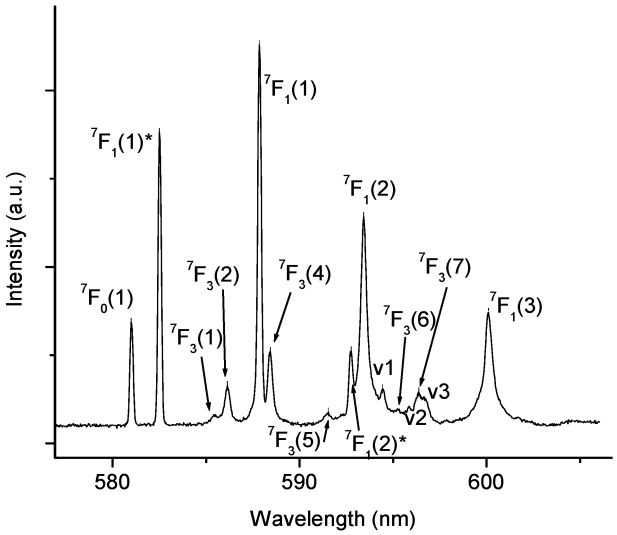

Figure 5. Emission spectrum (at 10 K) of 1% Eu^{3+}-doped Y_2O_3 prepared by the preformed sol route, PS1, under 488 nm excitation. The initial state is $^5D_1$ for the transitions to $^7F_3$, and $^5D_0$ for transitions to $^7F_0$ and $^7F_1$. Unstarred and starred bands correspond to C_2 and C_{3i} sites, respectively. The bands v_i ($i = 1-3$) correspond to vibronic structure of the $^5D_0 \rightarrow {}^7F_1$ transition; refer to the text.

different because the intensity ratio of the C_{3i} site band at 582.6 nm is much greater, being larger in the 0.1% Eu^{3+} sample compared with 1.0% Eu^{3+} and greater under 457.9 nm excitation compared with 488 nm.

The spectrum in Figure 5 shows the emission spectrum between 577 and 606 nm for the PS sample at low temperature and is more clearly resolved than other previously reported spectra of Y_2O_3:Eu^{3+} in this region.[35,36] The questions arise (i) why the C_{3i} site emission is relatively stronger relative to the C_2 site emission in the PS sample (Figure 5) than in the other samples (e.g., Figure 3) and (ii) why the emission from $^5D(3)_1$ (abbreviated to $^5D_1$ hereafter) is observed in the PS samples but not in the others. The answer to both concerns the higher dopant ion level (6%) in the FSP and CSP samples, which leads to more efficient energy transfer processes.

Regarding point i, Görller-Walrand et al.[37] have shown that the electric dipole intensity contribution to the $^5D_0 \rightarrow {}^7F_1$

transition is generally small, so that the total oscillator strength is independent of the site symmetry. In this case, the intensity of the emission from the C_2 site ($I[C_2]$) in Y_2O_3:Eu^{3+} should be 3 times that from the C_{3i} site ($I[C_{3i}]$), assuming a random distribution of Eu^{3+} ions in these sites. The measured intensity ratios $I[C_2]/I[C_{3i}]$ from Figures 2 and 4 are about 12:1 and 4:1, respectively. This indicates a preferential quenching of the C_{3i} emission in the CSP and FSP samples, due to the larger dopant ion concentrations in these samples, so that the energy transfer processes from C_{3i} to C_2 sites are enhanced. This energy transfer and back transfer from the C_{3i} site to the C_2 site has been thoroughly investigated for Y_2O_3:Eu^{3+}.[23,38,39] The $^5D_0$ energy level of Eu^{3+} at C_2 sites is 87 cm^{-1} lower than for the C_{3i} sites, so the former act as traps. The quenching has also been observed in the isostructural Lu_2O_3 by Zych et al.,[40,41] where emission from the C_{3i} site of Eu^{3+} decreases in relative intensity, compared with that from the C_2 site, at Eu^{3+} dopant ion concentrations in excess of 1%.

Weber[42] has pointed out that the C_2 site $^5D_0$ lifetime is fairly long (~0.9 ms) and independent of the Eu^{3+} concentration in Y_2O_3, whereas the $^5D_1$ lifetime is shorter and decreases from 120 μs for 0.1% Eu^{3+} to 50 μs for 10% Eu^{3+} dopant ion concentration. The nonradiative decay of $^5D_0$ is slow, since the highest phonon energy in Y_2O_3 is 596 cm^{-1},[43] and the energy gap[19] $^5D_0 - {}^7F_6$ is 11 580 cm^{-1} (i.e., 20 phonons). By contrast, the gap $^5D_1 - {}^5D_0$ is only 1714 cm^{-1} (3 phonons)[19] and although there are first-order selection rules that restrict $\Delta J = \pm 1$ nonradiative decay,[42] there are cross-relaxation pathways available in the more concentrated materials, such as the two-ion process

$$^5D_1\,(18\,930) + {}^7F_1\,(0) \rightarrow {}^5D_0\,(17\,216) + {}^7F_2\,(1380) + \text{phonon emission}\,(334) \quad (1)$$

or resonant three-ion processes. The $^5D_1$ emission from the C_2 site is therefore quenched at Eu^{3+} concentrations of a few percent.

Assignment of C_2 Site Energy Levels of Y_2O_3:Eu^{3+}. We have not made a thorough reinvestigation of the emission spectra of Y_2O_3:Eu^{3+} since our samples were powders. However, the derived energies of $^7F_0$ up to $^7F_4$ multiplets and of $^5D_0$ and $^5D_1$ are in general agreement with previous studies,[23,30,35,44] with energy differences of up to a few reciprocal centimeters resulting from different concentrations of Eu^{3+} employed in samples and different temperatures of measurement. By comparison of the 10 K PS spectrum of Y_2O_3:Eu^{3+} in Figure 5 with the time-resolved spectra,[45,46] the weaker bands, as marked, correspond to emission from $^5D_1$ to $^7F_3$. In fact, the assignment of one of the seven crystal field levels of $^7F_3$ is unclear in previous studies.[18,19,44] From our $^5D_0 \rightarrow {}^7F_3$ 10 K emission spectra (not shown), the terminal $^7F_3$ levels of the C_2 site are clearly assigned (in reciprocal centimeters) and numbered in order of increasing energy at 1845 (1), 1865 (2), 1905 (3), 2018 (5), 2128 (6), and 2158 (7). These energies closely match those derived from the $^5D_1$ emission, as identified in Figure 5. The $^5D_1 \rightarrow {}^7F_3(3)$ band is coincident with the intense $^5D_0 \rightarrow {}^7F_1(1)$ band. However, an additional level, $^7F_3(4)$, is clearly assigned at 1936 cm^{-1} (Figure 5), which is in agreement with the calculated energy (1946 cm^{-1}).[19] Furthermore, an unassigned band[44] in the 77 K absorption spectrum of Y_2O_3:Eu^{3+} at 1734 cm^{-1} is then readily assigned to the hot transition $^7F_1(1)$ [200 cm^{-1}] $\rightarrow {}^7F_3(4)$ [1936 cm^{-1}].

Assignment of Bands and Energy Levels for C_{3i} Sites. The Eu^{3+} ion at a C_{3i} site is octahedrally coordinated to oxygen, and the trigonal deviation from O_h symmetry results from the slightly different Eu−O distances of 0.226, 0.228, and 0.234 nm.[43] Various criteria, including the recording of emission lifetimes,[23,40,47] and selective excitation[35] including X-ray excitation[48] have been employed to distinguish the spectral features due to Eu^{3+} ions at C_{3i} sites from those due to C_2 sites.

TABLE 2: Energy Levels of Eu^{3+} at the C_{3i} Site in Cubic C-Y_2O_3 and C-Lu_2O_3

	energy (cm^{-1})				
$^{2S+1}L_J\,\Gamma(C_{3i})$	Y_2O_3[a]	Y_2O_3[b] exp	Y_2O_3[b] calc	Lu_2O_3[c] exp	Lu_2O_3[c] calc
$^7F_0\ A_g$	0	0	0	0	0
$^7F_1\ E_g$	132	448	447	401	402
$^7F_1\ A_g$	429	125	126	110	110
$^7F_2\ E_g$	830	839	821		
$^7F_2\ E_g$	948		1190		
$^7F_2\ A_g$	1184		955		
$^5D_0\ A_g$	17 302			17 283	17 283
$^5D_1\ E_g$	18 992			19 070	19 068
$^5D_1\ A_g$	19 084	18 996		18 979	18 980

[a] From this work and refs 23, 38, 39, 43, 47, 49, and 50. [b] From ref 8. [c] From ref 20.

The assignments of $^7F_1$ crystal field energy levels have been made from the $^5D_1$ and $^5D_0$ emission spectra. The latter required the identification of the electric hexadecapole-allowed electronic origin (or coincident defect site band) of the $^5D_0 \rightarrow {}^7F_0$ transition. This was accomplished by careful examination of associated vibronic structure in Y_2O_3:Eu^{3+} [23,49] and by investigation of pair electronic transitions in Eu_2O_3.[38] The determined energy of $^5D_0$ was 17 302 cm^{-1} in Y_2O_3:Eu^{3+} [23,49] and 17 321 cm^{-1} for Eu_2O_3.[38] Bloor and Dean[50] observed a band at 138 cm^{-1} in the range 10−250 cm^{-1} of the far-infrared absorption spectrum of Eu_2O_3, which was assigned to the C_{3i} site and is in agreement with the value of the lower $^7F_1$ crystal field level deduced from the optical spectrum.[38] In Figure 5, the second component of $^7F_1$ at the C_{3i} site, $^7F_1(2)$*, is clearly observed. This assignment is analogous to that in the spectrum of Gd_2O_3:Eu^{3+}.[2] Three very weak bands remain unassigned in Figure 5, and their excitation line−intensity dependence shows that they are associated with the C_{3i} site. These bands v_i ($i = 1-3$, Figure 5) correspond to vibronic structure of the $^5D_0 \rightarrow {}^7F_1$ transition, with derived vibrational energies 344, 383, and 409 cm^{-1}. Infrared-active [$T_u(T_h)$] vibrations have been reported at 343, 390, and 405 cm^{-1} in Y_2O_3.[50,51]

In a series of recent papers, the symmetry representations of the C_{3i} energy levels of $^7F_1$ and $^5D_1$, $^5D_2$ have been reassigned (Table 2) on the basis of two theoretical arguments.[3,8,20] The first of these reasons relied upon the predicted values of crystal field parameters from the point charge electrostatic model. In C_{3i} symmetry, the $J = 1$ multiplets comprise a nondegenerate (A_g) and a doubly degenerate (E_g) level. Out of the nine crystal field parameters B_q^k in C_{3i} symmetry, the crystal field splittings of the $J = 1$ multiplets depend almost exclusively upon B_0^2, due to the selection rule $k \leq 2J$. If this parameter is negative, then the levels of E_g symmetry have higher energy than those of A_g, whereas the reverse is true if B_0^2 is positive. Experimental data are available for only eight excited crystal field levels of Eu^{3+} at C_{3i} sites in Y_2O_3, so that the calculation[8] relied upon crystal field parameters calculated from an ab initio method.[52] In fact, it has long been recognized that the $^5D_1$ multiplet is one of the rogue multiplets, which is difficult to fit even in the full $4f^6$ calculation, and for example, 15 examples were quoted where the energy level fittings were poor.[53] Thus, the fit of only eight levels by use of nine crystal field parameters cannot be considered to provide reliable parameter values.

The second argument employed in the reassignment of crystal field levels was that plots of level baricenters should be linear. In fact the previous plot of experimental data for the $^7F_1$ baricenter against the $^5D_0$ level[54] exhibited considerable scatter. It has been pointed out that such deviations from the linear plot may indicate the occurrence of level perturbations,[55] and electron−phonon coupling[56] of low-lying multiplet levels such as Eu^{3+} $^7F_1$ [57] can cause such behavior. It is found that even the plot of the $^7F_1$ (360 cm^{-1}) against $^7F_2$ (1005 cm^{-1}) baricenter for $Cs_2NaEuCl_6$[58] does not lie near the straight line in the graph (Figure 3 of ref 8). Thus, although baricenter plots may be employed to indicate level perturbations, they cannot be used to make firm assignments of crystal field levels.

We now review the experimental evidence to substantiate the level assignments given in Table 2. First, it has been realized that the intensity of the transitions terminating upon the doubly and singly degenerate levels derived from $^7F_1(T_{2g})$ in O_h symmetry are roughly in the ratio of the degeneracies (2:1) for unpolarized radiation passing through randomly oriented material. Certainly, the transition terminating on the A level should not be more intense than that terminating on E. Hence, McCaw et al.[59] have assigned the A_{2g} and E_g states resulting from the tetragonal distortion of the $^7F_1(T_{1g})$ state in $Cs_2NaTbBr_6$ from the approximate intensity ratio 1:2 in the $^5D_4(A_{1g}) \rightarrow {}^7F_1(T_{1g})$ luminescence transition. Berry et al.[60] assigned E_g and A_g crystal field levels derived from $^5D_1(T_{1g})$ from the intensities in the 300 K emission excitation spectrum of the $^7F_0 \rightarrow {}^5D_1$ transition of trigonally distorted $Eu(AP)_6(ClO_4)_3$ (AP = antipyrine). Now, from the $^7F_0 \rightarrow {}^5D_1$ absorption spectrum of $Y_2O_3:Eu^{3+}$ (5 mol % Eu^{3+}),[30,35] the intensity ratio of the C_{3i} site transition terminating upon the level at 19 004 cm^{-1} to that at 19 093 cm^{-1} is 2.3:1, so that these terminal levels can be assigned to E_g and A_g, respectively. The relative intensities for the analogous bands are about 3:1 in $Lu_2O_3:Eu^{3+}$.[20] Also, concerning the $^5D_0 \rightarrow {}^7F_1$ transition, from Figure 5, the $^7F_1(1)^*$ band is clearly much stronger than the $^7F_1(2)^*$ band, so the levels at 132 and 429 cm^{-1} are assigned to E_g and A_g, respectively. Concerning the $^7F_2$ assignments, from the 15 K polarized electronic Raman spectrum,[43] the feature at 1184 cm^{-1} shows a dominant α_{xx} component, characteristic of A_g symmetry, which clearly distinguishes it from the polarizations of the bands at 830 and 948 cm^{-1}, assigned to E_g levels.

These symmetry assignments are consistent, since the splitting of both $J = 1$ levels is in the same order,[61] and the assignments agree with those of Heber and Köbler.[47]

Furthermore, the temperature−intensity dependence of the $^7F_1 \rightarrow {}^5D_0$ absorption lines[39] of $Y_2O_3:Eu^{3+}$ not only confirms the energy of the lowest $^7F_1$ level but also conclusively identifies the double degeneracy. The relative intensities of the hot band features in the absorption spectrum, corresponding to $^7F_1(1)^*$ and $^7F_1(1)$ in emission (Figure 5), from about 100 to 300 K were fitted according to[39]

$$\ln\left[\frac{I[^7F_1(1)^*]Z(C_{3i})}{I[^7F_1(1)]Z(C_2)}\right] = \ln c + \frac{1}{T}\left[\frac{200 - \Delta E}{k_B}\right] \qquad (2)$$

where ΔE is the energy $[^7F_1(1)^* - {}^7F_0^*]$ at the C_{3i} site, k_B is the Boltzmann constant, and T is the temperature in Kelvins, and the partition function, $Z(C_x)$, is given by

$$Z(C_x) = \sum_{i=0}^{\infty} g_i \exp(-\Delta E_i/k_B T) \qquad (3)$$

where g_i is the degeneracy of the ith crystal field level at energy ΔE_i above the ground state for the relevant Eu^{3+} site of symmetry C_x. The results gave $\Delta E = 132 \pm 5$ cm^{-1} and the degeneracy of the $^7F_1(1)^*$ level as 2.[39]

Table 2 includes the assignments recently made for Eu^{3+} doped into the isostructural Lu_2O_3 host,[20] where the sign of the parameter B_0^2 was also taken as negative in the calculation. For C_{3h}, D_3, and C_{3h} site symmetries of Eu^{3+} in $LaCl_3$,[62] $Na_3[Eu(ODA)_3]\cdot 2NaClO_4\cdot 6H_2O$,[63] and $[Eu(H_2O)_9](C_2H_5SO_4)_3$,[63] respectively, B_0^2 has been taken as positive. In octahedrally coordinated $Eu(AP)_6^{3+}$, with C_{3i} site symmetry the $J = 1$ levels are split into E_g and A_g, with the latter at higher energy.

Spectra and Cross-Relaxation Processes in $Y_2O_3:Er^{3+}$. The spectra of single crystals[64] and nanocrystals[65] of $Y_2O_3:Er^{3+}$ have been reported at 4.2 K. The derived energy levels have been fitted by crystal field analysis,[66] and the intensities have been calculated.[67] For reference, the literature energy levels of Er^{3+} in Y_2O_3 are shown[66] in Figure 2. The room-temperature optical emission spectra of nanocrystalline and bulk (10 mol % Er^{3+}) $Y_2O_3:Er^{3+}$ have recently been compared, with several conclusions as follows.[24,25] First, concerning the green emission, under 488 or 815 nm excitation, the emission from $^2H(2)_{11/2}$ (subsequently abbreviated as $^2H_{11/2}$), relative to that from $^4S_{3/2}$, was found to be stronger in the nanocrystals than in the bulk material. This was attributed to a greater distortion of the C_2 sites in the nanocrystals than in the bulk material.[24] Second, concerning the red emission, the intensity of bands at $\lambda > 670$ nm was found to be stronger for the bulk sample,[24] which was subsequently[25] explained to the occurrence of "vibronic transitions associated with the C_{3i} sites, which may be stronger in the bulk sample due to more favorable electron−phonon coupling". Third, the intensity of red emission, compared with green emission, was greater in the nanocrystals than in the bulk material, whether under blue or infrared excitation.[24,25] We now provide alternative explanations for these three observations.

Hot Bands in the Spectra. Our 488 nm excited green emission spectra of samples of $Y_2O_3:Er^{3+}$ (0.2−0.4 mol % Er^{3+}) prepared by the PS method are similar to the spectra reported by Newport et al.[68] All of the emission spectral lines can be assigned to Er^{3+} ions at C_2 sites, and the derived energies are in agreement with those reported by Kisliuk et al.[64] All crystal field energy levels correspond to Kramers doublets. The electric dipole transition intensity acquired by Er^{3+} at the C_2 sites therefore far outweighs the magnetic dipole intensity of the Er^{3+} ions at C_{3i} sites. Figure 6 shows the region between 530 and 565 nm, corresponding to emission from $^2H_{11/2}$ (labeled F) and $^4S_{3/2}$ (labeled E) to the $^4I_{15/2}$ electronic ground multiplet (labeled Z). The $^2H_{11/2}$ hot bands are considerably weaker than in the spectrum of the nanocrystals reported in refs 24 and 25. We attribute this to a higher (apparent or real) temperature in the nanocrystals. If thermal equilibrium exists, the temperature of the hot band level can be calculated from the simple formula:

$$R = k \exp(-\Delta E/k_B T) \qquad (4)$$

where R is the ratio of the hot band intensity (for the transition from level E2 or one of the F levels) to a cold transition originating from level E1, which has the same degeneracy; ΔE is the corresponding energy difference between E1 and the excited level; k, the ratio at infinite temperature, is related to the transition oscillator strengths and is assumed to be temperature-independent. For example, if we perform approximate estimations where R refers to the peak height intensity ratio of the transitions (E2 → Z7,Z8)/(E1 → Z7,Z8), ΔE is the energy (E2 − E1), then we can determine the constant k. In Figure 6, $R \sim 0.28$, $\Delta E \sim 86$ cm^{-1}, assuming no bulk sample heating by

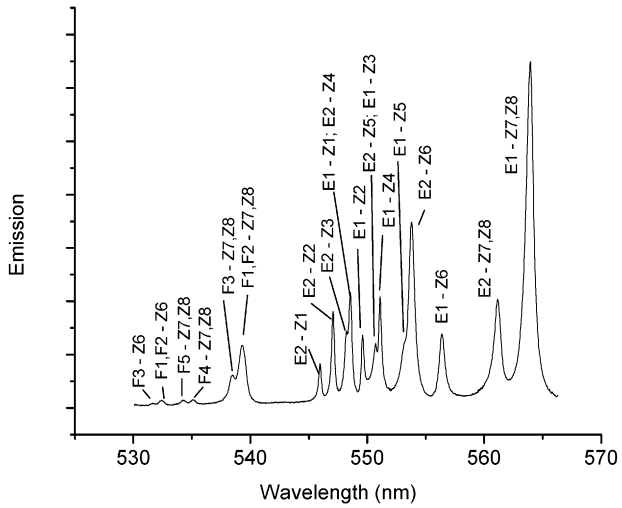

Figure 6. Room-temperature 488 nm excited emission spectrum of 0.8 mol % Er^{3+}-doped Y_2O_3 prepared by the preformed sol method. F, E, and Z represent $^2H_{11/2}$, $^4S_{3/2}$, and $^4I_{15/2}$, respectively, and the energy levels are numbered in increasing order of energy. In reciprocal centimeters, the levels are at 18 233 (E1) and 18 315 (E2); 19 041 (F1, F2), 19 072 (F3), and 19 187 (F4); and 0 (Z1), 38 (Z2), 76 (Z3), 89 (Z4), 158 (Z5), 258 (Z6), and 500 (Z7, Z8).

the laser, $T = 295$ K, and $k \sim 0.42$. A similar value ($k \sim 0.41$) is obtained from the 77 K spectrum of Y_2O_3:Er^{3+} in Kisliuk et al.[64] Then, using this value of k and analyzing the same bands in Figure 3a of ref 24 for nanocrystalline Y_2O_3:Er^{3+}, we find an effective temperature of about 365 ± 15 K, and the same result is obtained when we analyze the intensity ratio of the transitions (F1,F2 → Z7,Z8)/(E1 → Z7,Z8) in Figure 6 (or in Figure 4 of ref 68), compared with Figure 3a of ref 24. Thus the hot band temperature of the nanocrystals is effectively higher than that of the bulk material. Whether this hotness is due to the absence of particular phonons for thermalization or to the inability of a lattice wave to propagate through the nanomaterial, or to thermal energy produced at killer sites, or just to laser heating of the nanoparticles (these explanations not being mutually exclusive) is outside the scope of this study but has been investigated elsewhere.[13,69] The main point is that the intensity of hot bands from $^2H_{11/2}$ is much greater in the nanocrystals than in the bulk material, so that the population of this multiplet, relative to that of $^4S_{3/2}$, is greater than in the bulk material. This has important ramifications upon energy transfer processes, as discussed below.

This observation also explains the second point above, namely, why the intensity of bands at $\lambda > 670$ nm was found to be stronger for the bulk sample than for nanocrystals. Spectral analysis shows that the highest energy band in the red emission corresponds to $^4F_{9/2}$ (D5) → $^4I_{15/2}$ (Z1) at 647.8 nm and that other bands to high energy of that at 670 nm (D5 → Z8) are also hot.

Energy Transfer Processes. The intensity of emission was found to be greater for bulk Y_2O_3:Er^{3+} than for the nanocrystalline material, which is due to the presence of surface killer sites in the latter. Our concern here is the comparison of the relative intensities of green and red emission in these materials. The energy transfer process

$$^4S_{3/2}(E)\ (\text{ion } 1/2) + {}^4I_{15/2}(Z)\ (\text{ion } 2/1) \rightarrow {}^4I_{13/2}(Y)\ (\text{ion } 1/2) + {}^4I_{9/2}(B)\ (\text{ion } 2/1) + \Delta E \quad (5)$$

which can occur by ED−electric quadrupole (EQ) or ED−ED interaction, is near-resonant ($\Delta E \sim 10$ cm^{-1}) for initially populated E2 (18 318 cm^{-1}) and Z8 (510 cm^{-1}) crystal field levels and requires phonon absorption assistance of up to $\Delta E \sim 1240$ cm^{-1} for initially populated E1 and Z1 levels. On the other hand, the process

$$^2H_{11/2}(F)\ (\text{ion } 1/2) + {}^4I_{15/2}(Z)\ (\text{ion } 2/1) \rightarrow {}^4I_{13/2}(Y)\ (\text{ion } 1/2) + {}^4I_{9/2}(B)\ (\text{ion } 2/1) + \Delta E \quad (6)$$

can proceed without the absorption of energy and is effectively resonant, for example, F1 → Y4, Z1 → B2. Moreover, the energy transfer rate for eq 6 is much greater than that of eq 5, due to the large matrix element $\langle ^2H_{11/2}||U^{(2)}||^4I_{9/2}\rangle$, and can proceed by various multipolar interaction mechanisms including EQ−EQ.[70] Thus, when the excited level E2 of $^4S_{3/2}$ and especially when $^2H_{11/2}$ is populated, the energy transfer processes (eqs 5 and 6) will occur faster. Thus, from the hot band arguments above, these processes are expected to be more important in the nanomaterials than in the bulk Y_2O_3. The shortest C_2 site−C_2 site Er^{3+} distance is 0.35 nm, and the quenching of $^4S_{3/2}$ has been found to occur markedly for dopant ion concentrations of a few percent.[25]

A further cross-relaxation process

$$^2H_{11/2}(F)\ (\text{ion } 1/2) + {}^4I_{13/2}(Y)\ (\text{ion } 2/1) \rightarrow {}^4F_{9/2}(D)\ (\text{ion } 1/2) + {}^4I_{11/2}(A)\ (\text{ion } 2/1) \quad (7)$$

is resonant through several channels (for example, F1 + Y1 → D3 + A4) but has not previously been considered. Following processes 5 and 6, an ion is produced in $^4I_{13/2}$, so that process 7 can then occur if the neighbor is in $^2H_{11/2}$. Thus, eq 7 provides a mechanism for the feeding of $^4F_{9/2}$ and quenching of $^2H_{11/2}$, so that the intensity of red emission is greater in the nanocrystals than in the bulk material. The upconversion process

$$^4I_{11/2}(A)\ (\text{ion } 1/2) + {}^4I_{13/2}(Y)\ (\text{ion } 2/1) \rightarrow {}^4F_{9/2}(D)\ (\text{ion } 1/2) + {}^4I_{15/2}(Z)\ (\text{ion } 2/1) \quad (8)$$

also feeds $^4F_{9/2}$ and will be more efficient in the nanocrystals than in the bulk material because the populations of A and Y are higher, due to the greater importance of processes 5−7.

Conclusions

Several topics concerned with the luminescence of Y_2O_3:Ln^{3+} have been considered in this paper. The PS method is a simple and rapid method to prepare phosphors doped with Ln^{3+}. The particles are more uniformly shaped and filled when prepared by the FSP method than by CSP. The recent reassignments of the crystal field levels of Eu^{3+} doped into Y_2O_3 have been questioned on experimental grounds. Finally, energy transfer processes in nanoscale Y_2O_3:Er^{3+} have been rationalized.

Acknowledgment. This work was supported by the Hong Kong University Grants Council Research Grant CityU 1114/00P. We are indebted to Professor Seung Bin Park, Department of Chemical Engineering, Korea Advanced Institute of Science and Technology, for providing the FSP and CSP samples. We thank Dr. M. D. Faucher for useful discussions and Professor B. Tissue for sending reprints of his work.

References and Notes

(1) Laversenne, L.; Goutaudier, C.; Guyot, Y.; Cohen-Addad, M.; Boulon, G. *J. Alloys Compd.* **2002**, *341*, 214.

(2) Pires, A. M.; Santos, M. F.; Davolos, M. R.; Stucchi, E. B. *J. Alloys Compd.* **2002**, *344*, 276.

(3) Antic-Fidancev, E.; Hölsa, J.; Lastusaari, M. *J. Alloys Compd.* **2002**, *341*, 82.
(4) Klintenberg, M.; Edvardsson, S.; Thomas, J. O. *J. Alloys Compd*. **1998**, *275*−*277*, 174.
(5) Sharma, P. K.; Nass, R.; Schmidt, H. *Opt. Mater*. **1998**, *10*, 161.
(6) Serra, O. A.; Cicillini, S. A.; Ishiki, R. R. *J. Alloys Compd.* **2000**, *303*−*304*, 316.
(7) Cho, K. G.; Kumar, D.; Lee, D. G.; Jones, S. L.; Holloway, P. H.; Singh, R. K. *Appl. Phys. Lett.* **1997**, *71*, 3335.
(8) Antic-Fidancev, E.; Hölsa, J.; Lastusaari, M. *J. Phys. Condens. Matter* **2003**, *15*, 863.
(9) Schmechel, R.; Kennedy, M.; von Seggem, H.; Winkler, H.; Benker, A.; Winterer, M.; Hahn, H. *J. Appl. Phys.* **2001**, *89*, 1679.
(10) Meltzer, R. S.; Yen, W. M.; Zheng, H.; Feofilov, S. P.; Dejneka, M. J.; Tissue, B.; Yuan, H. B. *J. Lumin*. **2001**, *94*−*95*, 221.
(11) Sharma, P. K.; Jilavi, M. H.; Varadan, V. K.; Schmidt, H. *J. Phys. Chem. Solids* **2002**, *63*, 171.
(12) Song, H.; Chen, B.; Peng, H.; Zhang, J. *Appl. Phys. Lett*. **2002**, *81*, 1776.
(13) Peng, H.; Song, H.; Chen, B.; Wang, J.; Lu, S.; Kong, X.; Zhang, J. *J. Chem. Phys*. **2003**, *118*, 3277.
(14) Tissue, B. M.; Yuan, H. B. *J. Solid State Chem.* (in press).
(15) Eilers, H.; Tissue, B. M. *Chem. Phys. Lett*. **1996**, *251*, 74.
(16) Hong, K. S.; Meltzer, R. S.; Bihari, B.; Williams, D. K.; Tissue, B. M. *J. Lumin.* **1998**, *76*/*77*, 234.
(17) Meltzer, R. S.; Feofilov, S. P.; Tissue, B.; Yuan, H. B. *Phys. Rev*. **1999**, *B60*, R14012.
(18) Dexpert-Ghys, J.; Faucher, M. *Phys. Rev*. **1979**, *B20*, 10.
(19) Leavitt, R. P.; Gruber, J. B.; Chang, N. C.; Morrison, C. A. *J. Chem. Phys.* **1982**, *75*, 4775.
(20) Karbowiak, M.; Zych, E.; Hölsa, J. *J. Phys. Condens. Matter* **2003**, *15*, 2169.
(21) Tanner, P. A.; Sun, R. W. Y. *J. Mater. Sci.* **2001**, *36*, 2253.
(22) Hao, J.; Studenikin, S. A.; Cocivera, M. *J. Lumin.* **2001**, *93*, 313.
(23) Pappalardo, R. G.; Hunt, R. B. *J. Electrochem. Soc.* **1985**, *132*, 721.
(24) Capobianco, J. A.; Vetrone, F.; D'Alesio, T.; Tessari, G.; Speghini, A.; Bettinelli, M. *Phys. Chem. Chem. Phys*. **2000**, *2*, 3203.
(25) Capobianco, J. A.; Vetrone, F.; Boyer, J. C.; Speghini, A.; Bettinelli, M. *J. Phys. Chem. B* **2002**, *106*, 1181.
(26) Grill, A.; Schreiber, M. *Phys. Rev*. **1970**, *B1*, 2241.
(27) Mitric, M.; Onnerud, P.; Rodic, D.; Tellgren, R.; Szytula, A.; Napijalo, M. *J. Phys. Chem. Solids* **1993**, *54*, 967.
(28) Antic, B.; Mitric, M.; Rodic, D. *J. Phys.: Condens. Matter* **1997**, *9*, 365.
(29) Concas, G.; Muntoni, C.; Spano, G.; Bettinelli, M.; Speghini, A. *Z. Naturforsch.* **2001**, *A56*, 267.
(30) Forest, H.; Ban, G. *J. Electrochem. Soc.* **1971**, *118*, 1999.
(31) Kang, Y. C.; Roh, H. S.; Park, S. B. *Adv. Mater.* **2000**, *12*, 451.
(32) Seo, D. J.; Kang, Y. C.; Park, S. B. 2nd Asian Aerosol Conference, July 1−4, 2001, Pusan, Korea; Abstracts, p 121.
(33) Tanner, P. A.; Mak, C. S. K.; Kwok, W.-M.; Phillips, D. L.; Faucher, M. D. *Phys. Rev*. **2002**, *B66*, 165203.
(34) Judd, B. R. *Phys. Rev*. **1962**, *127*, 750.
(35) Forest, H.; Ban, G. *J. Electrochem. Soc.* **1969**, *116*, 474.
(36) Sharma, P. K.; Jilavi, M. H.; Nass, R.; Schmidt, H. *J. Lumin.* **1999**, *82*, 187.
(37) Görller-Walrand, C.; Fluyt, L.; Ceulemans, A.; Carnall, W. T. *J. Chem. Phys.* **1991**, *95*, 3099.
(38) Buijs, M.; Meyerink, A.; Blasse, G. *J. Lumin.* **1987**, *37*, 9.
(39) Heber, J.; Hellwege, K. H.; Köbler, U.; Murmann, H. *Z. Phys*. **1970**, *237*, 189.
(40) Zych, E.; Karbowiak, M.; Domagala, K.; Hubert, S. *J. Alloys Compd.* **2002**, *341*, 381.
(41) Zych, E. *J. Phys. Condens. Matter* **2002**, *14*, 5637.
(42) Weber, M. J. *Phys. Rev.* **1968**, *171*, 283.
(43) Schaack, G.; Koningstein, J. A. *J. Opt. Soc. Am.* **1970**, *60*, 1110.
(44) Chang, N. C.; Gruber, J. B. *J. Chem. Phys*. **1964**, *41*, 3227.
(45) Qiang, S.; Barthou, C.; Denis, J. P.; Pelle, F.; Blanzat, B. *J. Lumin.* **1983**, *28*, 1.
(46) Rhys Williams, A. T.; Fuller, M. J. *Comput. Enhanced Spectrosc*. **1983**, *1*, 146.
(47) Heber, J.; Köbler, U. *Luminescence of Crystals, Molecules and Solutions*; Williams, F., Ed.; Plenum: New York, 1973; p 379.
(48) Tola, P.; Retournard, A.; Dexpert-Ghys, J.; Lemonnier, M.; Pagel, M.; Goulon, J. *Chem. Phys.* **1983**, *78*, 339.
(49) Hunt, R. B.; Pappalardo, R. G. *J. Lumin.* **1985**, *34*, 133.
(50) Bloor, D.; Dean, J. R. *J. Phys. C: Solid State Phys*. **1972**, *5*, 1237.
(51) McDevitt, N. T.; Davidson, A. D. *J. Opt. Soc. Am.* **1966**, *56*, 636.
(52) Faucher, M.; Dexpert-Ghys, J. *Phys. Rev.* **1981**, *B24*, 3138.
(53) Moune, O. K.; Caro, P.; Garcia, D.; Faucher, M. *J. Less Common Metals* **1990**, *163*, 287.
(54) Antic-Fidancev, E. *J. Alloys Compd.* **2000**, *300*−*301*, 2.
(55) Tanner, P. A.; Mak, C. S. K.; Faucher, M. D. *J. Chem. Phys*. **2001**, *114*, 10860.
(56) Schaack, G. *Top. Appl. Phys*. **2000**, *75*, 24.
(57) Berry, M. T.; Kirby, A. F.; Richardson, F. S. *Mol. Phys.* **1989**, *66*, 723.
(58) Tanner, P. A.; Ravi Kanth Kumar, V. V.; Jayasankar, C. K.; Reid, M. F. *J. Alloys Compd*. **1994**, *215*, 349.
(59) McCaw, C. S.; Murdoch, K. M.; Denning, R. G. *Mol. Phys*. **2003**, *101*, 427.
(60) Berry, M. T.; Kirby, A. F.; Richardson, F. S. *Mol. Phys*. **1989**, *66*, 723.
(61) Görller-Walrand, C.; Binnemans, K. *Handbook on the Physics and Chemistry of the Rare Earths*; Gschneidner, K. A., Eyring, L., Eds.; Elsevier: Amsterdam, 1996; Chapt. 155, p 121.
(62) Morrison, C. A.; Leavitt, R. P. *Handbook on the Physics and Chemistry of Rare Earths*; Gschneidner, K. A., Eyring, L., Eds.; North-Holland: Amsterdam, 1982; Chapt. 46, p 494.
(63) Hopkins, T. A.; Bolender, J. P.; Metcalf, D. H.; Richardson, F. S. *Inorg. Chem.* **1996**, *35*, 5347.
(64) Kisliuk, P.; Krupke, W. F.; Gruber, J. B. *J. Chem. Phys*. **1964**, *40*, 3606.
(65) Matsuura, D. *Appl. Phys. Lett.* **2002**, *81*, 4526.
(66) Chang, N. C.; Gruber, J. B.; Leavitt, R. P.; Morrison, C. A. *J. Chem. Phys*. **1982**, *78*, 3877.
(67) Krupke, W. *Phys. Rev.* **1966**, *145*, 325.
(68) Newport, A.; Fern, G. R.; Ireland, T.; Withnall, R.; Silver, J.; Vecht, A. *J. Mater. Chem.* **2001**, *11*, 1447.
(69) Liu, G. K.; Zhuang, H. Z.; Chen, X. Y. *Nano Lett.* **2002**, *2*, 535.
(70) Chua, M.; Xia, S.; Tanner, P. A. *J. Phys. Condens. Matter* **2003**, *15*, 7423.